Computation of the noise radiated by a hot supersonic jet deflected in a flame trench

Adrien Langenais, François Vuillot, Julien Troyes, Hadrien Lambaré

Computation of the noise radiated by a hot supersonic jet deflected in a flame trench

A. Langenais,[1] F. Vuillot,[1] J. Troyes,[2] and H. Lambaré[3]
[1] *ONERA, University of Paris-Saclay, F-91123 Palaiseau, France*
[2] *ONERA, University of Toulouse, F-31055 Toulouse, France*
[3] *CNES, F-75612 Paris, France*

ABSTRACT:

This study aims to numerically investigate the noise radiated by a reduced-scale rocket engine jet at lift-off conditions including a flame trench. An over-expanded Mach 3.1 hot jet entering a flame duct where it impinges on a deflector before being guided in a horizontal duct, is considered. The computation is performed with a two-way coupled approach on unstructured grids. This methodology relies on a large-eddy simulation of the jet and the acoustic near field, associated with a full Euler simulation of the acoustic far field. The aerodynamic and acoustic results are compared to a previous computation involving the Ffowcs Williams and Hawkings approach and show a better agreement with the measurements conducted at the MARTEL facility. A more careful analysis of the pressure field suggests that the noise is strongly influenced by the flame trench geometry. Nonlinear propagation effects, natively taken into account by the full Euler solver, are finally highlighted and discussed. Based on appropriate metrics, a good agreement with the experiment is obtained.

DOI: https://doi.org/10.1121/10.0003759

I. INTRODUCTION

Rocket engine jets are known to generate a severe acoustic environment at lift-off which can be harmful to the launcher, its payload, and the launch pad structures. The noise from supersonic jets has been widely investigated[1]. Experimental studies were first conducted to identify the turbulent mixing noise, the broadband shock-associated noise and the Mach wave radiation[2]. Specific mechanisms such as nonlinearities and crackle[3,4], screech and feedback effects[5] and interaction with elementary obstacles[6,7] have been considered. Studies on reduced-scale launch pads[8–10] have helped to develop noise reduction devices for space applications. However, full-scale firings or experiments with realistic launch pad geometries are still challenging in terms of cost and quantitative measurement possibilities.

Semi-empirical models[11] provide low-cost jet noise level predictions but installation effects cannot be properly taken into account. Consequently, these approaches are gradually replaced by unsteady numerical simulations of the Navier-Stokes equations which give access to comprehensive flow information on complex configurations. The large-eddy simulation (LES) is now commonly used to compute hot supersonic jets with the associated acoustic fields[12] but a special attention must be paid to the nozzle exit boundary layer state[13,14]. Impinging effects have also been numerically examined. To mention a few, Gojon *et al.*[15] and Dauptain *et al.*[16] have studied feedback loops, Brehm *et al.*[17] have detailed noise generation mechanisms with an inclined plate, Nonomura *et al.*[18,19] have investigated plate distance and angle effects on noise sources, and Tsutsumi *et al.*[9,10] have focused on obstacle shapes and launch pad design.

The acoustic far field can be extrapolated at low cost by an integral method[20] as applied in practical configuration of impinging jet[9,21]. The assumptions of a homogeneous propagation medium and linear acoustic regime are, however, required. Therefore, this approach might be unsuitable for space applications where the acoustic field is subject to complex installation effects and nonlinear propagation effects induced by high noise levels[3,22,23]. A coupling procedure between a flow solver and a computational aeroacoustics solver based on the resolution of the full Euler equations is a relevant alternative strategy. One-way coupling methods have been successfully applied to jet noise[22,24,25] but are unable to deal with feedback phenomena or secondary flows. Recently, a two-way coupling procedure between fully unstructured Navier-Stokes and Euler solvers has been developed, validated[26] then applied to free[27] and impinging jet[28] cases.

The present study aims at extending this two-way coupling methodology to a realistic launch pad configuration in order to gain more insight into the aeroacoustic mechanisms. The noise from an over-expanded Mach 3.1 hot jet at lift-off conditions is simulated in the presence of a model flame trench. The paper is organized as follows. In Section II, the case parameters and the corresponding available database are described, as well as the numerical procedure encompassing the solver features, the coupling method, the grid design, and the turbulence tripping. The aerodynamic fields are discussed in Section III. The main flow properties are commented on. Comparisons with a previous computation and the available measurements from the equivalent free jet case are then exhibited.

The acoustic results are presented in Section IV focusing on instantaneous fields and comparisons with noise measurements and a Ffowcs Williams and Hawkings computation. Discussions about the flame trench effects on the spatio-frequency content of the noise and the nonlinear propagation effects are then proposed. The relevance of several nonlinearity metrics is addressed. Concluding remarks are provided in Section V.

II. SIMULATION PARAMETERS

A. Case definition and database

1. Jet conditions

An over-expanded hot jet with a design Mach number $\mathrm{M}_d = u_e/c_e = 3.1$ and a Reynolds number $\mathrm{Re}_D = u_e D/\nu_e = 3 \times 10^5$ is considered, where the subscript e refers to the jet exit conditions on the centerline. The equivalent ideally expanded Mach number is $\mathrm{M}_j = 2.8$. The jet results from a hydrogen-air combustion at a total pressure $p_i = 30 \times 10^5\,\mathrm{Pa}$ and a total temperature $T_i = 1750\,\mathrm{K}$. The equivalent propellant gas has a specific heat ratio $\gamma = 1.3$. The jet is exhausted from a convergent-divergent nozzle with an exit diameter $D = 60\,\mathrm{mm}$ at the velocity $u_e = 1670\,\mathrm{m/s}$ under the conditions $T_e/T_\infty = 2.6$ and $p_e/p_\infty = 0.6$. The ambient medium is air at $\gamma = 1.4$, $T_\infty = 293.15\,\mathrm{K}$ and $p_\infty = 1 \times 10^5\,\mathrm{Pa}$.

2. Experimental set-up

These jet conditions are chosen to match an experimental study conducted at the MARTEL semi-anechoic facility[29]. The test bench aims at investigating free or impinging supersonic jet noise and allows the set up of reduced-scale launch pads at lift-off conditions. The configuration of interest in this work consists of a cylindrical body, containing the motor and the nozzle, mounted above a single-duct flame trench as represented in Figure 1. The flame trench is composed of a vertical square duct with a circular inlet and a 45° inclined deflector followed by a horizontal square duct. The nozzle exit is located $1D$ above the trench inlet. The trench exit is situated at $x = 20.45D$ away from the jet axis.

3. Measurement and simulation database

No aerodynamic measurements have been performed for this configuration. Nevertheless, a one point-two components laser Doppler velocimetry (LDV) campaign has been operated for a free jet with an identical nozzle and close generating conditions[27,30]. These measurements include the profiles of mean axial and radial velocities, root mean square fluctuating axial and radial velocities, along the jet centerline and radially at four axial locations, $1D$, $3D$, $3.67D$, and $6D$ away from the nozzle exit.

The present flame trench configuration involves numerous near field and far field noise measurements. The arrays marked as C, F, and G in Figure 1(a) consist of three standalone microphones C1, C2, and G3 in addition to four rings of sensors F1, G1, F2, and G2, each composed of four microphones spaced every $\Delta\varphi = 90°$ in azimuth. The diameters of the rings F and G centered on the motor axis are, respectively, $4.0D$ and $10.5D$. Four arcs of microphone denoted $\mathrm{AZ}n \mid n \in [1, 2, 4, 5]$, with a radius of $70D$ centered on the intersection point of the jet axis with the ground, are located at azimuths $\varphi \in [-22.5°, 67.5°, 157.5°, 247.5°]$. On each arc, the microphones are spaced by an observation angle of $\Delta\theta = 11.25°$. The microphone recording bandwidth is 50 kHz.

A previous computation of this flame trench configuration has been also carried out[31] which complement the database. The same flow solver was used but on a different mesh and no turbulence tripping strategy was implemented. The acoustic far field was treated with the Ffowcs Williams and Hawkings (FW-H) approach.

B. Numerical procedures

1. Overall set-up

The jet and the acoustic near field are simulated by solving the Navier–Stokes equations by LES in the region hereafter denoted zone Z1 and the acoustic far field is computed solving the full Euler equations in zone Z2 as illustrated in Figure 1. The solvers are coupled through two disjoint surfaces. The first one, denoted S1, links the circular section of the motor body to the square section of the trench top. The second one, denoted S2, extends from the square section of the horizontal duct just before the exit and gradually widens downstream up to a semi-circular section in the plane of the domain external boundary. The nozzle exit plane is positioned at the altitude $y_{nzl} = 6.54D$ in the Cartesian coordinate system and the nozzle-to-plate distance is $h_{imp} = 6.72D$. In this paper, the cylindrical coordinate system (y, r_{cyl}, φ), centered on the jet axis and the origin $(y_{nzl}, 0, 0)$, or the spherical coordinate system $(r_{sph}, \theta, \varphi)$, centered on the intersection of the jet axis with the ground, are sometimes preferred for convenience of analysis. The convergent-divergent nozzle, the motor body, and the ground are explicitly included in the computation. The whole domain extends in a parallelepiped of dimension $158.3 \times 150.0 \times 93.7D^3$. The external boundaries of Z2 are all set as non-reflective conditions except for the ground and the motor body, set as purely reflective walls. The downstream boundary of Z1 is set as a non-reflective subsonic outlet.

The widening rate of the surface S2 has to be carefully chosen to ensure that the hot and turbulent exhaust flow is contained within Z1. Indeed, feeding the acoustic solver with hot propellant gas can cause spurious noise and robustness problems. At the same time, the volume dedicated to the Navier–Stokes solver has to be limited for computational cost reasons. Consequently, an additional mean flow of 20 m/s in the direction $\vec{x}$ has been arbitrarily imposed in the whole domain to ensure that this secondary flow is maintained within Z1, but limited repercussions on the acoustic field are assumed (see the interference discussed in section IV B).

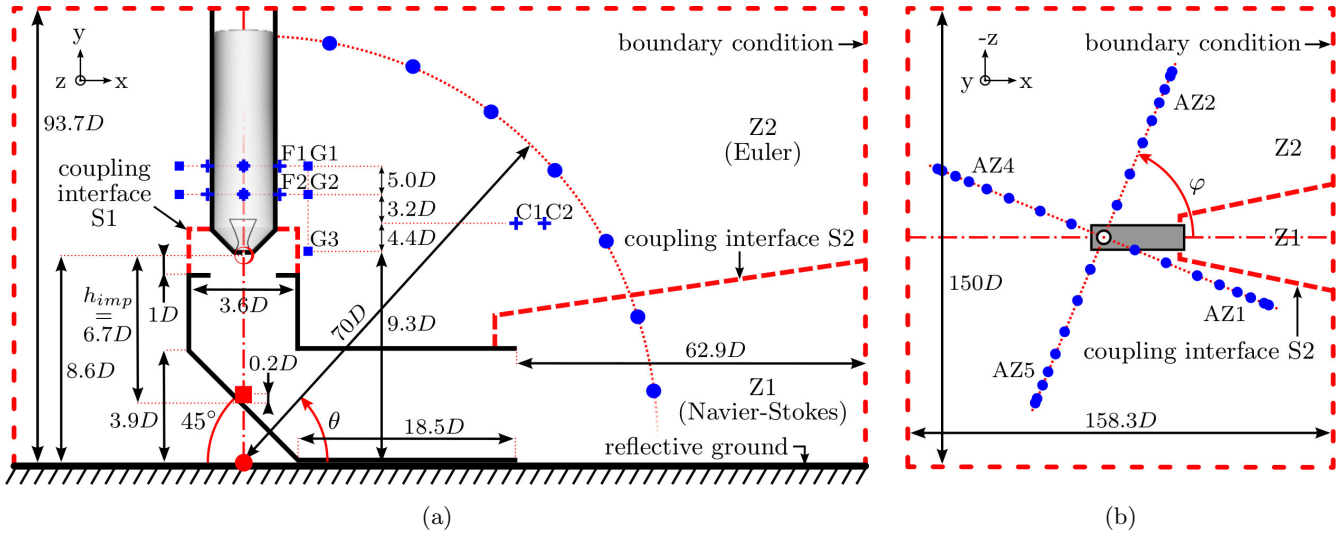

FIG. 1. (Color online) Configuration set-up in side view (a) and top view (b). The blue squares and crosses indicate the near field microphones and the blue dots the far field microphones. The origin is marked as a red square in Cartesian coordinates, as a red circle in cylindrical coordinates, and as a red dot in spherical coordinates.

2. Flow solver

The computation in Z1 is carried out with the multi-physics platform CEDRE which operates on general unstructured elements[32,33]. The filtered compressible Navier–Stokes equations are solved with a Smagorinsky subgrid-scale model with a constant value $C_s = 0.1$. No wall model is used but the van Driest damping function is implemented. The specific heat is defined by a 7^{th} order polynomial for air and is set constant for the propellant gas. Species viscosity is calculated according to the Sutherland law. The time integration is performed with an implicit 2^{nd} order Runge–Kutta scheme associated with a GMRES linear system solver. The flux is calculated with a 2^{nd} order k-exact method[34] and a Harten–Lax–van Leer contact flux-difference splitting scheme[35].

3. Acoustic solver

The unstructured computational aeroacoustics code SPACE[36] is used in Z2. The full Euler equations are solved *via* a nodal discontinuous Galerkin (DG) method using high-order polynomial elements. The propagation medium is air, whose thermodynamic properties are set constant with $\gamma = 1.4$. The time integration is achieved with an explicit 2^{nd} order Runge–Kutta scheme and elements up to the 4^{th} order are employed. The DG method in SPACE allows to locally adapt the element orders. This feature is called order mapping or p-adaptation. Characteristic-based non-reflective boundary conditions and a shock-capturing scheme are also implemented.

4. Two-way coupling

The flow and the acoustic solvers are two-way coupled at the interfaces S1 and S2. The cell localization and the data exchange are handled by the CWIPI coupling library[32,37]. Conformal tetrahedral meshes without overlapping are considered at the interfaces. The coupling algorithm consists of locating the boundary cells on each side of the interfaces, then calculating and exchanging at every time step the quantities required by the other solver. A more complete description of the coupling features can be found in reference[26]. Since the flow and the acoustic computations are, respectively, second and fourth order accurate, the coupling interface can be seen as an accuracy discontinuity which could generate spurious noise and numerical instabilities. This issue is treated by locally adapting element orders close to the interface on the SPACE side. The small size cells imposed by the flow solver at the interface in Z1 are set to the second order in Z2. Moving away from the interface, the cell size increases and the element orders quickly rise to the third, then to the fourth order. This method ensures a smooth transition from the numerical accuracy point of view, without reducing the computation order since the flow solution remains second order accurate.

5. Turbulence tripping

The jet exit conditions have been found critical to properly reproduce the shear layer thickness, its spread rate, and the generated noise[13,38,39]. In order to control the initial turbulence level, the flow can be either seeded with synthetic fluctuations[14,39,40] or geometrically disturbed at the nozzle wall *via* surface roughness[41] or obstacles[42]. In the present work, a $0.01D$ high axisymmetric step is added in the convergent nozzle, $1.37D$ upstream of the nozzle exit plane. Combined with a sufficiently refined grid along the nozzle downstream wall, the tripping yields peak fluctuating velocity levels u'_y/u_e of about 7% in the exit plane as shown below in Figure 5(b).

6. Validation

All aspects of the numerical procedure have been validated independently. Academic cases involving acoustics have been directly simulated with the flow solver CEDRE[26]. In practical simulations, the required spatial resolution in terms of point per wavelength (PPW) has been found to be PPW = 20 for a proper wave propagation on unstructured tetrahedral meshes[27,33]. The acoustic solver SPACE has been similarly evaluated[36,43]. A spatial resolution of PPW = 5 at the 4^{th} order, higher than the minimal requirement, is used here. The resulting numerical dissipation is approximately 10^{-3} dB per wavelength at the cut-off frequency which is on the order of the atmospheric viscous damping[44]. The two-way coupling between the solvers has been also validated on a series of appropriate cases including propagation of high amplitude waves and shocks[26].

The methodology has then been applied to the free jet case. The effect of the step on the turbulence tripping inside the mixing layer has been quantified independently of the mesh refinement[27] and the best geometrical parameters have been adopted here. The effect of the acoustic method, i.e., the full Euler solver or the FW-H approach, on the far field noise computation has been examined both in case of a coarse mesh[30] and a refined mesh[27]. A significant grid effect on the noise levels has been found and is discussed in the references. The Euler solver compared to the FW-H approach has given better predictions in terms of noise directivity as well as frequency content and statistical properties of the pressure time histories. This fully validated new approach is used in the present work. To illustrate the benefits on the present configuration, it will be compared to a similar computation performed with the previous approach (no turbulence tripping and FW-H extrapolation).

7. Grid parameters

The unstructured grid used in the previous computation is depicted in Figure 2(a) and is denoted grid A. It is composed of 74×10^6 tetrahedra and prisms, where 6.7×10^6 cells were devoted to the nozzle, 32.7×10^6 to the trench, 24.9×10^6 to the external field extending up to the FW-H surface, and 9.9×10^6 beyond as buffer zone. The edge of the tetrahedra was typically $a = 28 \times 10^{-3} D$ inside the nozzle, $33 \times 10^{-3} D \leq a \leq 73 \times 10^{-3} D$ inside the trench, and $a = 97 \times 10^{-3} D$ outside. The prisms height at the trench walls was constant with $h = 7 \times 10^{-3} D$.

The new mesh presented in Figure 2(b), denoted grid B, is unstructured and mainly composed of tetrahedra. It includes 117×10^6 cells in Z1 for the Navier–Stokes computation, where 31.0×10^6 cells are devoted to the nozzle, 55.2×10^6 to the trench, 30.9×10^6 outside, and 93×10^6 cells in Z2 for the Euler computation, or, equivalently, 1.8×10^9 degrees of freedom when the high-order elements are taken into account. The characteristic cell sizes according to the geometrical type are given at key locations in Table I. Note that the equivalent cell diameter is defined by $d_{cell} = 6V/A$ where V and A are, respectively, the volume and the total face area of the cell. For a regular tetrahedron of edge a, d_{cell} is then equal to the diameter of the inscribed sphere $a\sqrt{6}/6$.

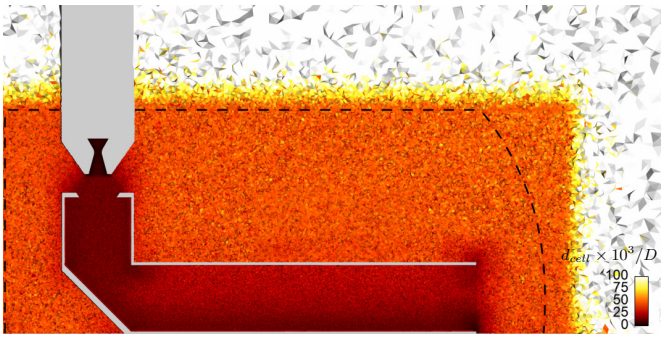

(a)

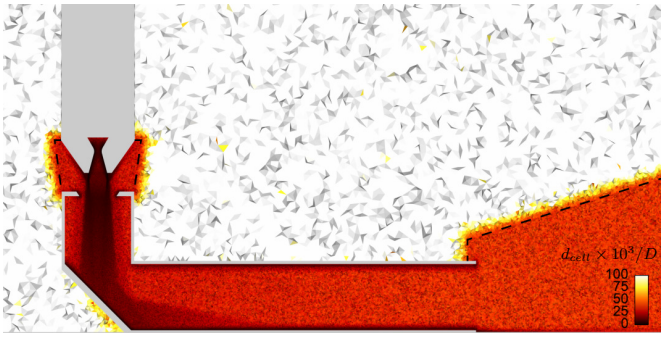

(b)

FIG. 2. (Color online) Mesh visualization in the plane $\vec{x}\vec{y}(z = 0)$ colored by d_{cell} for grid A (a) and grid B (b). The FW-H integration surface on grid A and the coupling interface on grid B are represented as a dashed black line.

Particular attention is paid to the refinement of the step and the downstream nozzle wall with hexahedra. The azimuthal resolution at the lips is $2\pi/\Delta\varphi \simeq 800$ points. The trench walls are discretized with ten layers of prisms. The impingement point on the deflector and the wall immediately downstream are especially refined. The tetrahedra size inside the jet gradually increases downstream of the lips. The overall acoustic cut-off frequency St_c of the simulation, with $\mathrm{St} = fD/u_e$ the Strouhal number, is estimated from the maximum cell size imposed in the refined domain, which extends up to the far field microphones of the arrays AZn. This results in $\mathrm{St}_c \simeq 0.24$ considering $d_{cell} = 35 \times 10^{-3} D$ and PPW = 20 in the Navier–Stokes zone Z1, and $\mathrm{St}_c \simeq 0.23$ considering $d_{cell} = 150 \times 10^{-3} D$ and PPW = 5 in the Euler zone Z2. In comparison, grid A was coarser than grid B, providing an azimuthal resolution at the lips of 400 points, thicker prisms inside the trench and finally an acoustic cut-off frequency of $\mathrm{St}_c \simeq 0.2$.

The computation has been performed on 1736 Broadwell processors of the ONERA's parallel scalar cluster. The total cost is 4×10^6 CPU hours. The simulation provides an established aerodynamic state duration of $1110D/u_e = 230D/c_\infty$ and a minimum established

TABLE I. Characteristic sizes of the hexahedra at the nozzle walls (top), the prisms at the flame trench walls (mid), and the tetrahedra inside the jet, the flame trench and in the outer acoustic field (bottom).

	step	throat	divergent	lips
$y_{nzl} - y$	$-1.37D$	$-1.16D$	$-0.17D$	$-0.0D$
$\Delta y \times 10^3/D$	2.3	1.6	3.3	2.5
$r\Delta\varphi \times 10^3/D$	2.1	1.6	3.5	3.8
$\Delta r \times 10^3/D$	0.5	0.3	0.8	0.8
$d_{cell} \times 10^3/D$	1.0	0.7	1.4	1.6

	imp. point	lower wall		upper wall	
x	$0.0D$	$1.8D$	$20.45D$	$1.8D$	$20.45D$
$h \times 10^3/D$	2.2	1.7	6.7	10.0	10.0
$a \times 10^3/D$	5.0	8.3	25.0	50.0	33.3
$d_{cell} \times 10^3/D$	2.7	3.0	10.4	17.7	14.7

	lips	shear layer	jet axis		Z1	Z2
$y_{nzl} - y$	$0.0D$	$1.0D$	$0.0D$	$1.33D$	N/A	N/A
$a \times 10^3/D$	2.5	8.3	25.0	16.7	85.7	367.0
$d_{cell} \times 10^3/D$	1.0	3.4	10.2	6.8	35.0	150.0

acoustic state duration of $835D/u_e = 175D/c_\infty$ as exploitable time, which can be limited in terms of temporal convergence for low frequencies. The minimum accessible frequency in the far field is then $\mathrm{St}_{min} = 1.2 \times 10^{-3}$ but in practice, a relevant low frequency bound considering a few periods is set to $\mathrm{St}_{min} = 1 \times 10^{-2}$.

III. FLOW FEATURES

A time-resolved simulation of the transient flow immediately after the motor ignition has been first conducted on grid B. The primary and secondary flows in the near field are roughly established within $420D/u_e$ of time. A mass flow rate of 1.28 kg/s is injected by the nozzle. Once the mean trench inflow and outflow are balanced, the entrained air accounts for more than half of the total mass flow rate of 2.7 kg/s inside the duct. Similar mass flow rates are recovered on grid A. Instantaneous vorticity fields after the transient period are displayed in the three cut planes $\vec{x}\vec{y}(z=0)$, $\vec{y}\vec{z}(x=0)$ and $\vec{y}\vec{z}(x=10D)$ in Figure 3(a). They show the shear layer development and the turbulent structures downstream of the impingement. Significant vorticity levels are found close to the nozzle exit thanks to the turbulence tripping strategy.

The mean Mach field is depicted in the same three cut planes in Figure 3(b). The impingement of the supersonic jet induces a strong plate shock followed by a wall jet showing a secondary shock train as obtained by Nonomura *et al.*[19] for instance. The plate shock yields

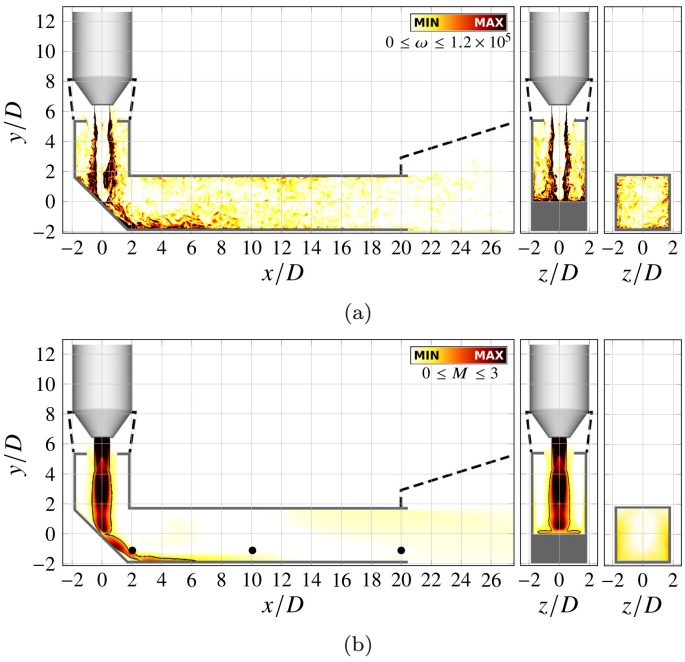

FIG. 3. (Color online) Instantaneous vorticity field (a) and mean Mach number field (b) in the planes $\vec{x}\vec{y}(z=0)$, $\vec{y}\vec{z}(x=0)$, and $\vec{y}\vec{z}(x=10D)$. The sonic line is represented as a solid black line and the coupling interface as a dashed black line.

a subsonic flow immediately downstream, which explains the local shrinkage of the sonic line. The junction of the deflector with the bottom wall can be seen as a second impingement and generates another shock. The wall jet also spreads on the sides and goes up the lateral walls.

Given that no aerodynamic measurements have been performed on this specific configuration, the velocity field is compared with the LDV data acquired for the free jet at a nearly identical motor operating point[27]. In the following, all positions and lengths indicated by an asterisk are made dimensionless by the jet exit diameter D_e. Note that the simulated jet is slightly separated in the vicinity of the nozzle lips, leading to an effective jet diameter $D_e = 0.97D$. The dimensionless nozzle-to-plate distance then becomes $h^*_{imp} = 6.95$.

The mean axial velocity and the fluctuating (RMS) velocity along the jet centerline are reported in Figures 4(a) and 4(b), respectively. The mean velocity in the present simulation on grid B shows analogous values with the measurements but a shifted second shock. The early drastic velocity decrease matches with the first shock which turns out to be a small Mach disk. Its location on the axis is similar to that of the free jet but the following shock cell is substantially longer. A length of $L^*_{1^{st}\,shock} = 3.0$ is obtained while $L^*_{1^{st}\,shock} = 2.6$ is found in the free jet case, whether based on the experiment, the simulation[27] or the analytical model of Tam and Tanna's[45]. The difference can be attributed to both the ambient air suction and confinement effects in the vertical duct. Knowing that the geometrical tripping only seeds fluctuations in the vicinity of the nozzle wall,

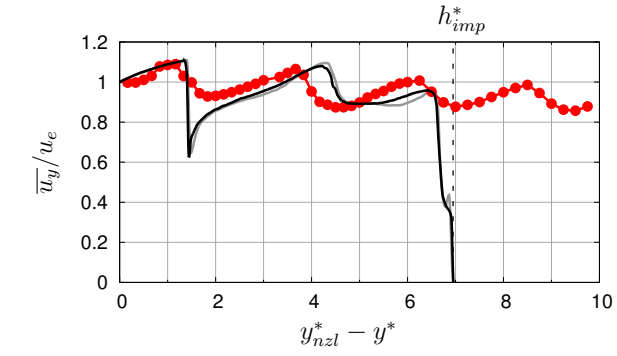

(a)

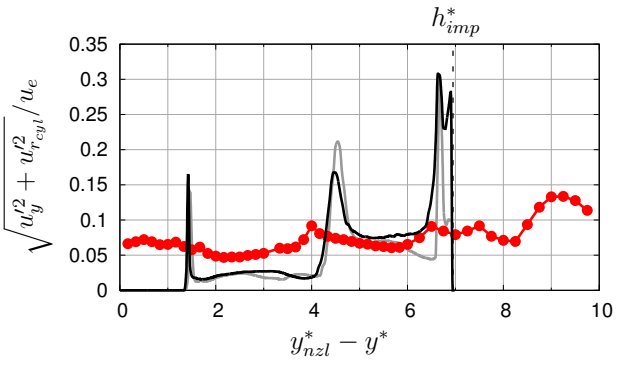

(b)

FIG. 4. (Color online) Profiles along the jet centerline of dimensionless mean axial velocity (a) and fluctuating velocity (b) for the free jet experiment (red line with dots), the previous simulation on grid A (solid gray line), and the present simulation on grid B (solid black line).

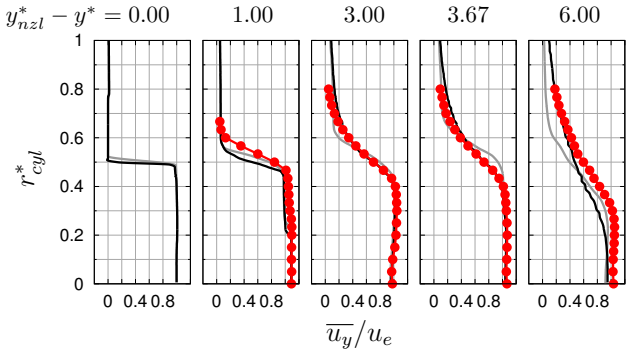

(a)

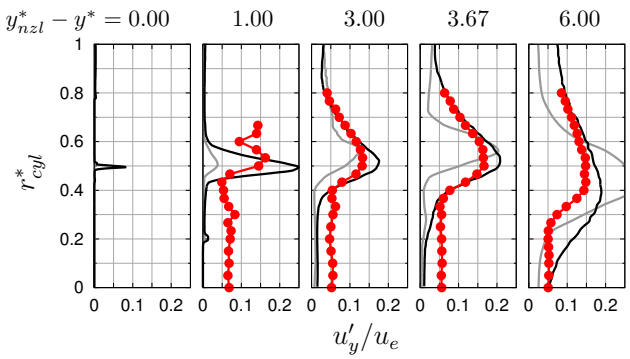

(b)

FIG. 5. (Color online) Radial profiles of dimensionless mean axial velocity (a) and fluctuating axial velocity (b) for the free jet experiment (red line with dots), the previous simulation on grid A (solid gray line), and the present simulation on grid B (solid black line).

the simulation shows a lack of turbulence on the axis at the nozzle exit compared to the experiment as already stressed in past studies[30,46]. A better agreement is obtained downstream of the Mach disk thanks to fluctuations generated by the triple-points[27]. The mean and fluctuating velocities decrease downstream of the plate shock at $y^*_{nzl} - y^* = 6.7$ and finally fall to zero at the impingement point $y^*_{nzl} - y^* = h^*_{imp}$. Small discrepancies are found between grids A and B regarding the centerline which suggests limited grid effects.

Radial profiles of the mean axial velocity and the fluctuating axial velocity are depicted in Figures 5(a) and 5(b), respectively. It should be noticed that the jet is no longer axisymmetric at the last location $y^*_{nzl} - y^* = 6$ because of the impingement. Consequently, the corresponding profiles are plotted without azimuthal averaging, only taking into account the radius $x > 0$ along the $\vec{x}$-axis. The mean velocity on grid B remains close to the measurements and slows down just before the impingement. The turbulence tripping allows significant fluctuation levels in the emerging shear layer leading to a reasonable agreement downstream. On the contrary, the fluctuating velocity is strongly underestimated on grid A near the nozzle exit, leading to a narrower shear layer, an abrupt laminar-turbulent transition and finally an overestimation of turbulence intensity at $y^*_{nzl} - y^* = 6$. The improvement provided by the turbulence tripping and the mesh refinement on grid B appears necessary for a proper turbulence development. Near the impingement at $y^*_{nzl} - y^* = 6$, the fluctuation rate in the shear layer close to the jet core increases faster in the simulations than in the free jet case. It is likely that the confinement and the recirculating flows in the vertical duct favor the penetration of turbulent structures into the potential core as occurring on the snapshot in Figure 3(a).

The properties of turbulence are examined by calculating power spectral densities (PSD) of the velocity field. The dB scale is computed with a reference value of 1 m/s. The axial velocity spectra inside the jet shear layer in Figure 6 indicate that the turbulence has still not reached an homogeneous and isotropic state before the impingement since the $\mathrm{St}^{-5/3}$ slope of the Kolmogorov's law is not clearly followed. Downstream of the impingement inside the horizontal duct, PSDs of the velocity u_x above the bottom wall at the locations marked by black dots in Figure 3(b), are given in Figure 7. The spectra fit the $\mathrm{St}^{-5/3}$ slope over a decade. The range of the turbulent energy cascade gradually shifts to lower frequencies when moving downstream, reflecting the formation of larger turbulent structures as expected.

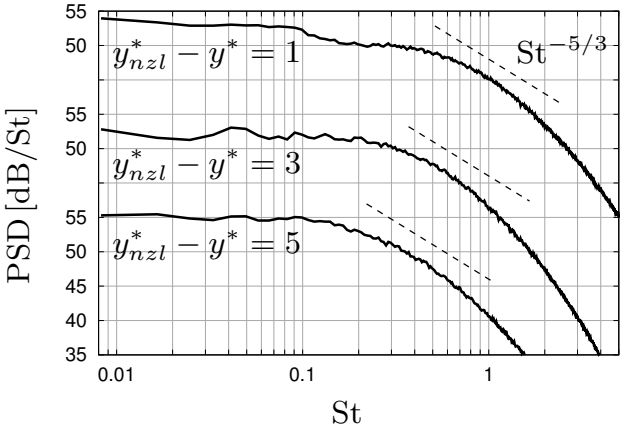

FIG. 6. Azimutally averaged PSDs of the axial velocity u_y inside the shear layer at $r_{cyl} = 0.5D$, at three altitudes, for the present simulation on grid B. The Kolmogorov's law is represented as a dashed black line.

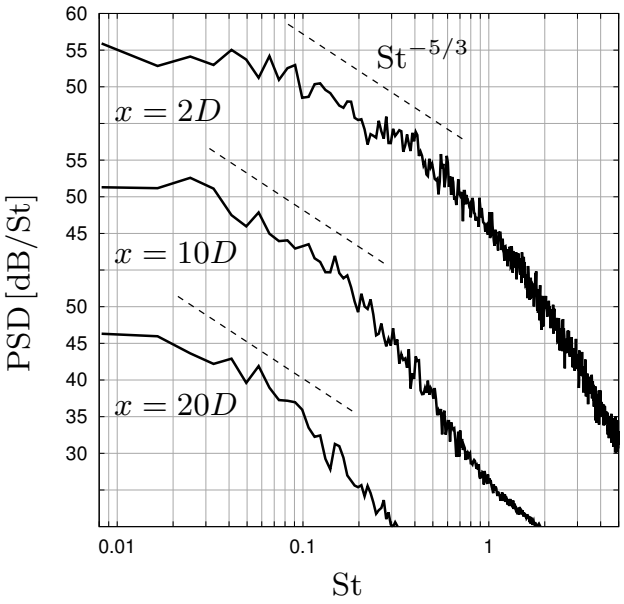

FIG. 7. PSDs of the velocity u_x inside the flame trench, $0.9D$ above the bottom wall, at the three black dot locations marked in Figure 3(b), for the present simulation on grid B. The Kolmogorov's law is represented as a dashed black line.

IV. ACOUSTICS

Because the flow and the acoustic field inside the flame trench are particularly complex due to the geometry, the noise sources are hard to distinguish. Looking at the analyses from the literature dealing with jets impinging on inclined plates[7,17,19], it is assumed that the noise generation mechanisms mainly consist of the Mach wave radiation from the free jet, including the reflections on the deflector, the noise associated with the interaction of large turbulent structures with the plate and tail shocks, and the Mach wave radiation from the wall jet.

A. Instantaneous fields

Instantaneous pressure fields in the four cut planes $\vec{x}\vec{y}(z = 0)$, $\vec{y}\vec{z}(x = 0)$, $\vec{x}\vec{z}(y = 20D)$, and $\vec{y}\vec{z}(x = 20D)$ in Figure 8 illustrate the wave propagation in the whole refined domain of grid B. A proper continuity can be observed at both coupling interfaces S1 and S2, indicated by black dashed lines. The noise is emitted mostly from the trench exit area and to a lesser extent from the spacing between the nozzle and the trench inlet. The wave pattern in Figure 8(c) suggests a quite directive source near the location $(x, y, z) = (22D, 0, 0)$. If these coordinates are taken as reference point, the angle range of dominant radiation roughly extends from 55° to 85° in the plane $\vec{x}\vec{y}(z = 0)$ and from ±40° to ±80° in the plane $\vec{x}\vec{z}(y = 20D)$ as represented by red dotted lines, respectively, in Figures 8(a) and 8(c). Directions of dominant radiation do not stand out so clearly in the two transverse planes in Figures 8(b) and 8(d). Since it is not obvious on the snapshots, it has been verified that the noise emanating from the spacing between the nozzle and the trench comes from both the free jet, especially early Mach waves reflected on the trench top, and the waves escaping from the trench inlet. The resulting acoustic field fed by the two sources is subject to complex reflection, diffraction, and interference phenomena. In addition, the waves diffracted by the trench exit edges radiate toward the motor and can be reflected, diffracted, or re-transmitted to the Navier–Stokes zone through S1. The wavelengths longer than the motor body diameter, i.e. $\mathrm{St} < 0.05$ approximately, are especially diffracted. Consequently, significant interference are expected in the $x < 0$ region, behind the motor body and the vertical part of the trench. Moreover, the noise from the trench exit can interfere with its own reflections and also directly with the noise from the spacing between the nozzle and the trench inlet. Finally, shadow zones are noticeable, in the $+\vec{x}$ direction downstream of the trench exit, and in the $-\vec{x}$ direction behind the motor body.

B. Comparison with noise measurements

The acoustic results are first compared to the experiment regarding the overall sound pressure levels. The OASPL is calculated by integrating the PSD over the resolved frequency range $0.01 \leq \mathrm{St} \leq 0.23$. The dB scale is computed with a reference value of 2×10^{-5} Pa. The microphone locations as well as the definition of the angles θ and φ are reminded in Figure 8.

The levels at the near field microphones on the arrays C, F, and G are provided in Table II. Very good agreement is obtained at most of the locations in the present Euler simulation on grid B, with an absolute difference of 1.1 dB on average. In comparison, the FW-H extrapolation from grid A provides a reasonable absolute difference of 2.3 dB on average. The field symmetry is respected to within 1 dB when considering the microphones at azimuths $\varphi = \pm 90°$. Drops in level in the shadow zone at the azimuth $\varphi = 180°$ behind the motor body are found

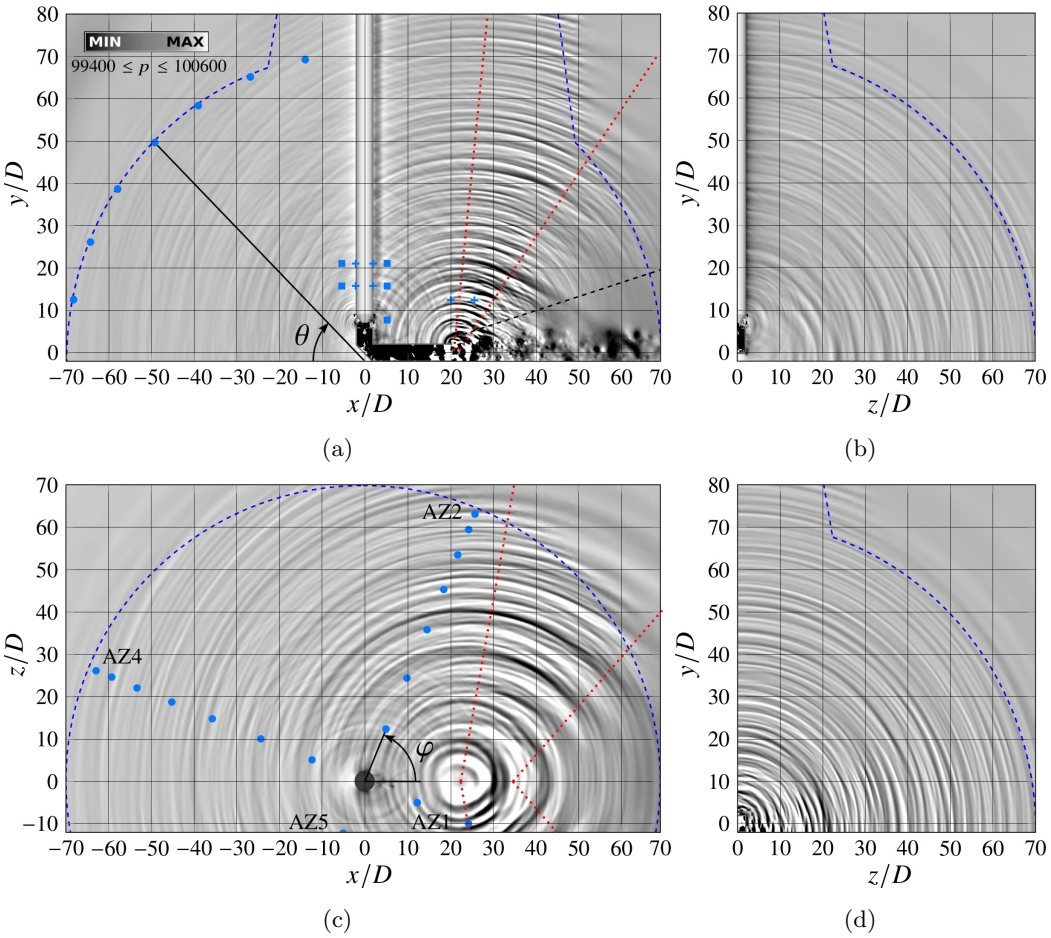

FIG. 8. (Color online) Instantaneous pressure field in the planes $\vec{x}\vec{y}(z = 0)$ (a), $\vec{y}\vec{z}(x = 0)$ (b), $\vec{x}\vec{z}(y = 20D)$ (c), and $\vec{y}\vec{z}(x = 20D)$ (d). The estimated angle range of dominant radiation is indicated by dotted red lines. The coupling interface is represented as a dashed black line and the boundary of the refined computational domain as a dashed blue line. The blue squares and crosses indicate the near field microphones and the blue dots the far field microphones.

at F1c, F2c, G1c, and G2c while the FW-H approach fails to capture this behavior since the installation effects are not properly taken into account. Note that this drop is not recovered experimentally at G1c. It could be explained by slight discrepancies in interference patterns or by additional installation effects since the motor body is not a perfect cylinder in the experiment. A limited overestimation of about 2 dB is predicted at the closest points from the main noise source, i.e., C1 and C2.

Regarding the far field microphones, the OASPLs are plotted in Figure 9 against the observation angle θ along the arrays AZn. Both the OASPL from bounded and full experimental spectra are displayed for completeness. The directivity shapes are well reproduced in the Euler simulation on AZ1 and AZ2 with peak angles at $\theta_{peak} \simeq 50°$ and $\theta_{peak} \lesssim 20°$, respectively. These maximums are associated with the directive noise from the trench exit previously highlighted. The largest deviations on these two arrays compared to the experiment is +1.7 dB on AZ2 at $\theta = 11.25°$. The levels are significantly lower on AZ4 and AZ5. The fine variations are more difficult to simulate because of the complex reflection, diffraction, and interference effects in the $x < 0$ region. The maximum deviation reaches −2.8 dB on AZ4 at $\theta = 78.75°$ but the overall accordance remains satisfactory. The FW-H simulation gives very good estimations on AZ4 and AZ5 with a 2.3 dB maximum deviation. On the contrary, the peak angle is shifted by 10° on AZ1 and the levels are overestimated by 2 to 5 dB on AZ2. The Euler computation on grid B is clearly superior in these regions.

The acoustics are now compared in terms of PSDs. Unless otherwise stated, the Welch method is used with a 50% overlapping and a natural windowing as recommended for broadband signals. The number of blocks is adjusted according to each exploitable time to obtain the same frequency sampling $\Delta\mathrm{St} = 7 \times 10^{-3}$. Figure 10 includes the PSDs on the arrays AZn at $\theta = 45°$ while Figure 11 gives the PSDs on AZ1 at all observation angles where measurements are available. The PSDs at the locations C1 and G3 are also provided in Figure 10.

The experimental data exhibit recurrent broadband peaks roughly centered on $\mathrm{St} \in [0.015, 0.03, 0.06, 0.12, 0.175, 0.22]$, particularly visible at C1 and G3 or at AZ1($\theta = 78.75°$). Except for some poorly captured peaks, for example, $\mathrm{St} \simeq 0.03$ at AZ4($\theta = 45°$), the major trends and peaks are finely predicted by the present simulation. In the $x > 0$ region, the PSDs at C1, C2, and AZ1($\theta \geq 45°$) point out that the noise from the trench exit, that is radiating in the dominant direction as well as at larger angles, mainly contains mid frequencies $0.05 < \mathrm{St} < 0.20$ in particular around $\mathrm{St} = 0.06$ and $\mathrm{St} = 0.12$. On the contrary, the noise emitted at shallow angles is dominated by lower frequencies, in particular around $\mathrm{St} = 0.015$ and $\mathrm{St} = 0.03$. The drop in level around $\mathrm{St} = 0.04$ found on AZ4 at $\theta = 45°$ as well as on the upper half of the array (not shown) is certainly the

TABLE II. OASPL in the near field at the microphone arrays C, F, and G. All levels are integrated over the range $0.01 \leq \mathrm{St} \leq 0.23$. The measurement at F1b suffers from a spurious noise. The microphone G3 is located inside the FW-H surface.

array	micro	azimuth φ	OASPL				
			experiment	previous simul.(FW-H)	deviation from exp.	present simul.(Euler)	deviation from exp.
C	C1	$+0°$	141.9 dB	144.4 dB	+2.5 dB	143.7 dB	+1.8 dB
	C2	$+0°$	148.4 dB	149.4 dB	+1.0 dB	150.7 dB	+2.3 dB
F	F1a	$+0°$	133.7 dB	130.4 dB	−3.3 dB	132.8 dB	−0.9 dB
	F1b	$+90°$	N/A	130.4 dB	N/A	130.4 dB	N/A
	F1c	$+180°$	125.7 dB	129.8 dB	+4.1 dB	124.8 dB	−0.9 dB
	F1d	$-90°$	131.1 dB	130.6 dB	−0.5 dB	131.4 dB	+0.3 dB
	F2a	$+0°$	134.5 dB	130.6 dB	−3.9 dB	133.2 dB	−1.3 dB
	F2b	$+90°$	131.1 dB	132.9 dB	+1.8 dB	132.4 dB	+1.3 dB
	F2c	$+180°$	126.7 dB	131.3 dB	+4.6 dB	126.8 dB	+0.1 dB
	F2d	$-90°$	131.4 dB	132.0 dB	+0.6 dB	132.5 dB	+1.1 dB
G	G1a	$+0°$	130.3 dB	131.1 dB	+0.8 dB	130.7 dB	+0.4 dB
	G1b	$+90°$	128.2 dB	130.7 dB	+2.5 dB	128.8 dB	+0.6 dB
	G1c	$+180°$	128.2 dB	129.5 dB	+1.3 dB	125.4 dB	−2.8dB
	G1d	$-90°$	128.3 dB	131.1 dB	+2.8 dB	129.2 dB	+0.9 dB
	G2a	$+0°$	131.3 dB	131.9 dB	+0.6 dB	132.0 dB	+0.7 dB
	G2b	$+90°$	129.5 dB	132.5 dB	+3.0 dB	130.7 dB	+1.2 dB
	G2c	$+180°$	127.0 dB	131.1 dB	+4.1 dB	127.9 dB	+0.9 dB
	G2d	$-90°$	129.7 dB	131.7 dB	+2.0 dB	130.7 dB	+1.0 dB
	G3	$+0°$	134.5 dB	N/A	N/A	135.9 dB	+1.4 dB

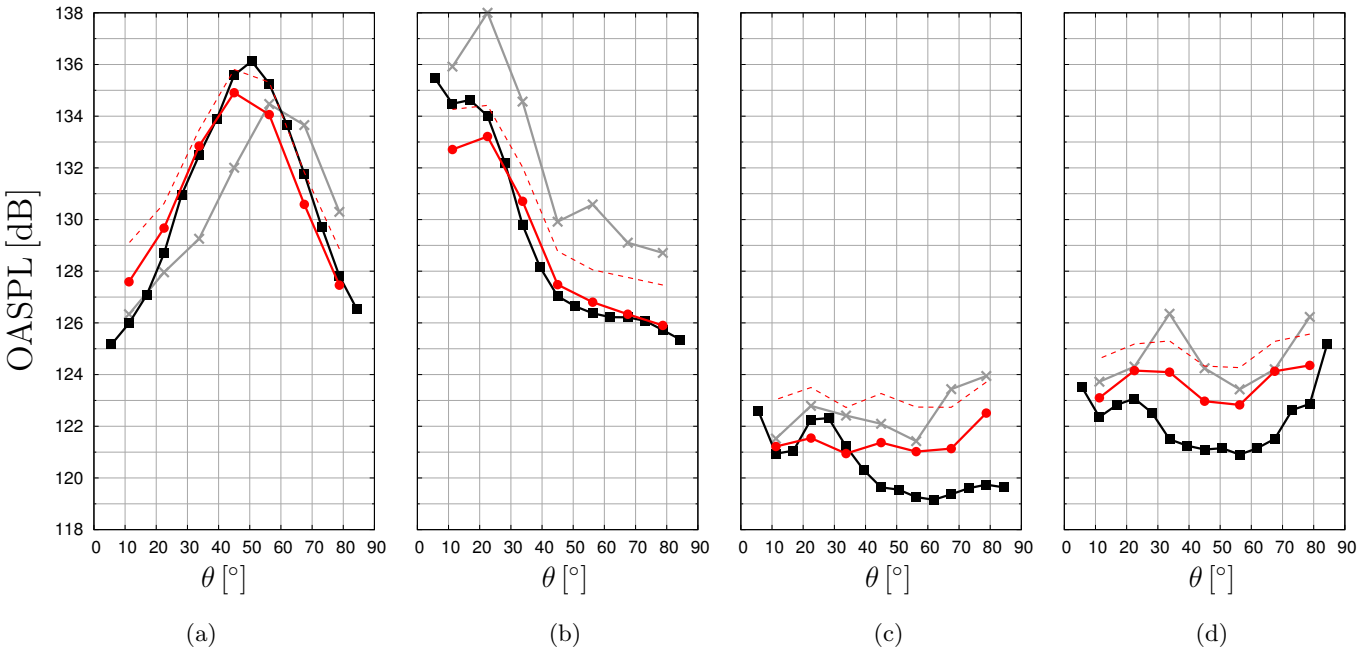

FIG. 9. (Color online) OASPL as a function of the observation angle θ on the arrays AZ1 (a), AZ2 (b), AZ4 (c), and AZ5 (d) for the experimental data integrated over the range $0.01 < \mathrm{St} < 0.23$ (red line with dots) and integrated over the full spectrum (dashed red line), the previous simulation with the FW-H approach (gray line with crosses), and the present simulation with the Euler solver (black line with squares) both integrated over the range $0.01 < \mathrm{St} < 0.23$.

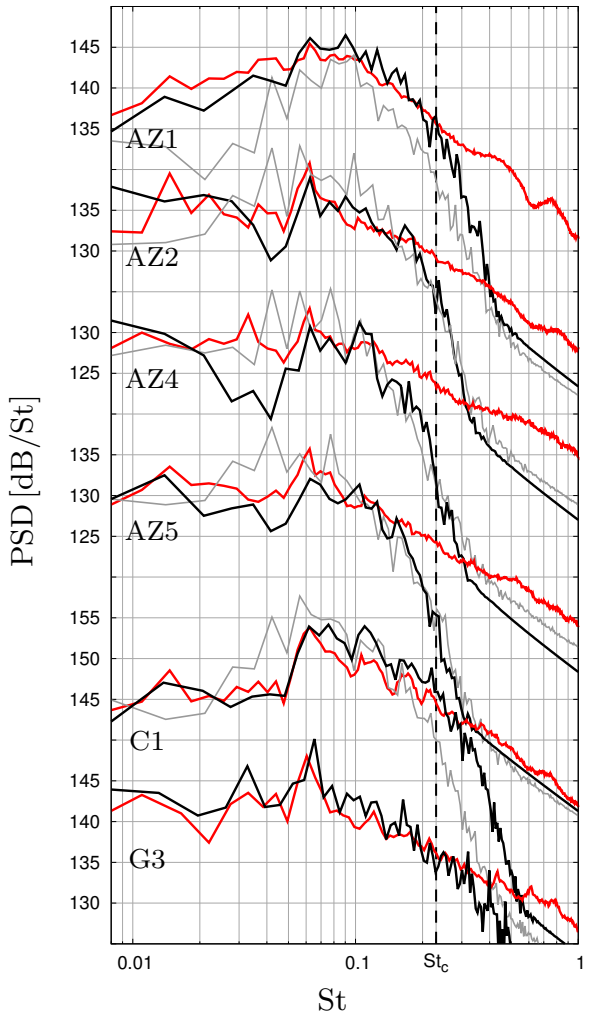

FIG. 10. (Color online) PSDs of the pressure on the arrays AZn at the observation angle $\theta = 45°$ and on the microphones C1 and G3, for the experimental data (solid red line), the previous simulation with the FW-H approach (solid gray line), and the present simulation with the Euler solver (solid black line). The estimated cut-off frequency $\mathrm{St}_c = 0.23$ is represented as a dashed black line.

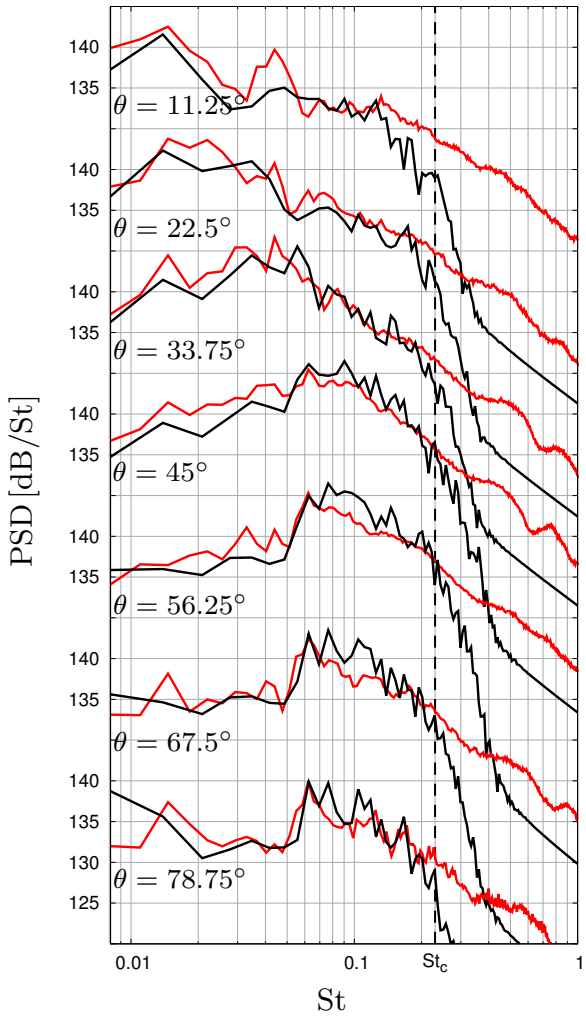

FIG. 11. (Color online) PSDs of the pressure on the array AZ1 at all the observation angles θ for the experimental data (solid red line) and the present simulation with the Euler solver (solid black line). The estimated cut-off frequency $\mathrm{St}_c = 0.23$ is represented as a dashed black line.

result of an interference because the corresponding wavelength is close to the motor body diameter. The difference with the experiment and the previous computation could be a side effect of the motor body modeled as a perfect cylinder, or of the free stream imposed in the present computation which shifts the interference patterns.

The PSDs calculated from the FW-H simulation in Figure 10 show more discrepancies with the experiment. The levels at mid frequencies $0.04 < \mathrm{St} < 0.1$ are overestimated in most of the spectra, in particular on AZ2, AZ4, and AZ5 at all angles (not shown), while they are underestimated at low frequencies $\mathrm{St} < 0.3$, especially at shallow angles on AZ1 and AZ2. The difference is less pronounced in the near field for the arrays C, F, and G in the region $x > 0$ which suggests a major effect of the acoustic method on the far field propagation.

C. Flame trench effects on the radiated noise

It can be shown that the flame trench tends to reduce the overall radiated noise level. The acoustic power integrated over a duct section is approximated by

$$\mathcal{P}_{ac} = \int \frac{\overline{p'^2}}{\overline{\rho}.\overline{c}}\,\mathrm{d}y\mathrm{d}z \qquad (1)$$

where $\overline{p'^2} = \overline{p(t)^2} - \overline{p(t)}^2$ is the square fluctuating pressure and $\overline{c}$ the mean speed of sound. This quantity is plotted against the location in the horizontal duct in Figure 12. The section surface is constant and equal to $0.046\,\mathrm{m}^2$. The trends are similar on both grids A and B, showing a decreasing acoustic power when moving downstream of the main noise sources. This effect is attributed to the interaction between the wave propagation and the turbulent mixing inside the duct.

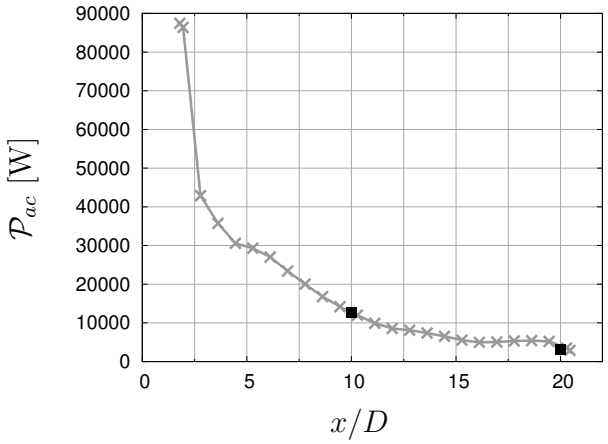

FIG. 12. Estimated acoustic power inside the horizontal duct for the previous simulation on grid A (gray line with crosses) and the present simulation on grid B (black squares).

The spatio-frequency content of the acoustic field is also affected by the flame trench, obviously because of the jet impingement on the deflector which deeply modifies the dominant noise sources, but also due to the duct geometry. The pressure field inside the horizontal duct is represented as a spatial spectrogram in Figure 13. The spectrogram is built from PSDs calculated at $1111 \times 5 \times 5$ scatter points, equally distributed in each direction of the horizontal duct. The PSDs are averaged over the 5×5 points in the y and z directions, then plotted against x/D. The frequency sampling is $\Delta\mathrm{St} = 2.6 \times 10^{-3}$. A Hann windowing has been used here to improve the peak capture. In the first half of the duct, the pressure fluctuations are strongly contaminated by the broadband turbulence spectrum. The very high levels at $x = 2D$, $3.8D$, and $5.7D$ are associated with structures convected by the wall jet through the tail shocks as similarly obtained by Brehm *et al.*[17]. However, several peaks also emerge from the noise downstream. For $x > 12D$, peaks clearly appear at precise frequencies, especially in the range $0.05 < \mathrm{St} < 0.16$. An explanation could be the excitation of the transverse acoustic modes of the square duct. The corresponding frequencies are given by

$$\mathrm{St}_m(x) = \frac{m\bar{c}(x)}{2L} \times \frac{D_e}{u_e} \tag{2}$$

where m is the mode order, L the duct width or height, and $c(x)$ the mean speed of sound at the location x. The first four modes are calculated, taking $c(x)$ equal to the time-averaged speed of sound along the x-axis, and superimposed as blue dashed lines in Figure 13. In the second half of the duct, the modes are consistent with the peaks on the spectrogram around $\mathrm{St} = 0.05$, 0.11, and 0.16. In practice, c is heterogeneous inside the duct implying that this approach is approximate. Moreover, longitudinal duct modes could also be excited and a feedback on the jet would be possible in the vertical part. All these phenomena could justify the other peaks on the spectrogram around $0.06 < \mathrm{St} < 0.08$, $\mathrm{St} = 0.12$ and even at the lower frequencies $\mathrm{St} = 0.015$ or 0.025.

As a consequence, the radiated noise outside the trench is expected to contain peaks at specific frequencies. In the near field, such features have been highlighted earlier, for instance for the microphones C1 and G3 in Figure 10, respectively close to the trench exit and to the trench inlet. The broadband peaks around $\mathrm{St} \in [0.015, 0.03, 0.06, 0.12, 0.175, 0.22]$ are linked to the behavior emphasized on the spectrogram inside the duct. Similar results are found in the far field. To get an overview, the fields of OASPL and peak frequency of the pressure spectrum are depicted in the planes $\vec{x}\vec{y}(z = 0)$ and $\vec{y}\vec{z}(x = 20D)$ in Figure 14. The directions of dominant radiation are associated with the highest peak frequencies (light yellow-white) along narrow corridors. The mid peak frequencies $0.05 < \mathrm{St} < 0.16$ (orange-yellow) which are predominant on the spectrogram, are recovered in a major part of the $x > 0$ region, at large angles in the plane $\vec{x}\vec{y}(z = 0)$ and at all angles in the side directions. The lowest peak frequencies (black-red) are finally found at shallow angles in the $x > 0$ region and over a wide area in the $x < 0$ region because of the shadow zone behind the motor body. This distribution is consistent with the PSDs on the arrays AZn in Figures 10 and 11. Note that the high levels at low frequency in the Navier–Stokes zone downstream of the trench exit are due to aerodynamic perturbations. In conclusion, the whole acoustic field seems marked by the frequencies favored by the duct geometry.

D. Nonlinear effects

At high acoustic levels, the propagating waves can experience cumulative nonlinear effects such as waveform steepening, shock formation and shock coalescence. The steepening can be seen as an energy shift to higher frequencies in the spectrum. Quantifying these effects is therefore essential to correctly determine the jet noise properties and to assess the usefulness of solving the full Euler equations in the far field. Given the OASPLs reported in Figure 14(a), with levels higher than 160 dB at the trench exit and higher than 140 dB on a large section of the coupling interface S2, nonlinear effects can be expected in the far field even at such a reduced-scale[27]. A set of appropriate metrics from the literature is then introduced, including the Goldberg number Γ, the skewness Sk, the kurtosis Kt, the wave steepening factor WSF, and the average steepening factor ASF. The skewness and the kurtosis are defined for a discrete signal s by

$$Sk(s) = \frac{\overline{s^3}}{\sigma^3}, \quad Kt(s) = \frac{\overline{s^4}}{\sigma^4} \tag{3}$$

where $\overline{s^3}$ and $\overline{s^4}$ are the third and fourth statistical moments, $\overline{s}$ the mean, and σ the standard deviation of the signal. These metrics measure the distortion of the signal probability distribution. Their values are equal to $Sk(s) = 0$ and $Kt(s) = 3$ in case of a Gaussian signal and increase regarding the pressure signal when the

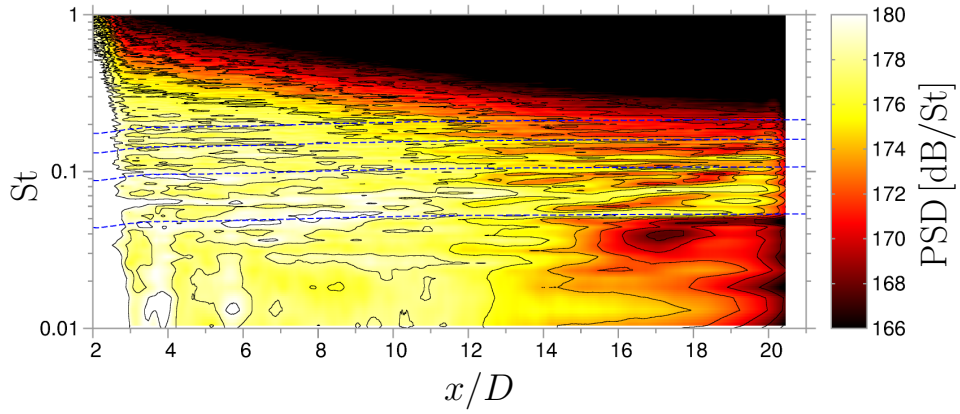

FIG. 13. (Color online) Averaged spectrogram of the pressure inside the horizontal duct as a function of x. Iso-contours are plotted every 2 dB/St as solid black lines. The estimated frequencies of the transverse acoustic modes $m \in [1, 2, 3, 4]$ of the square section are represented as dashed blue lines.

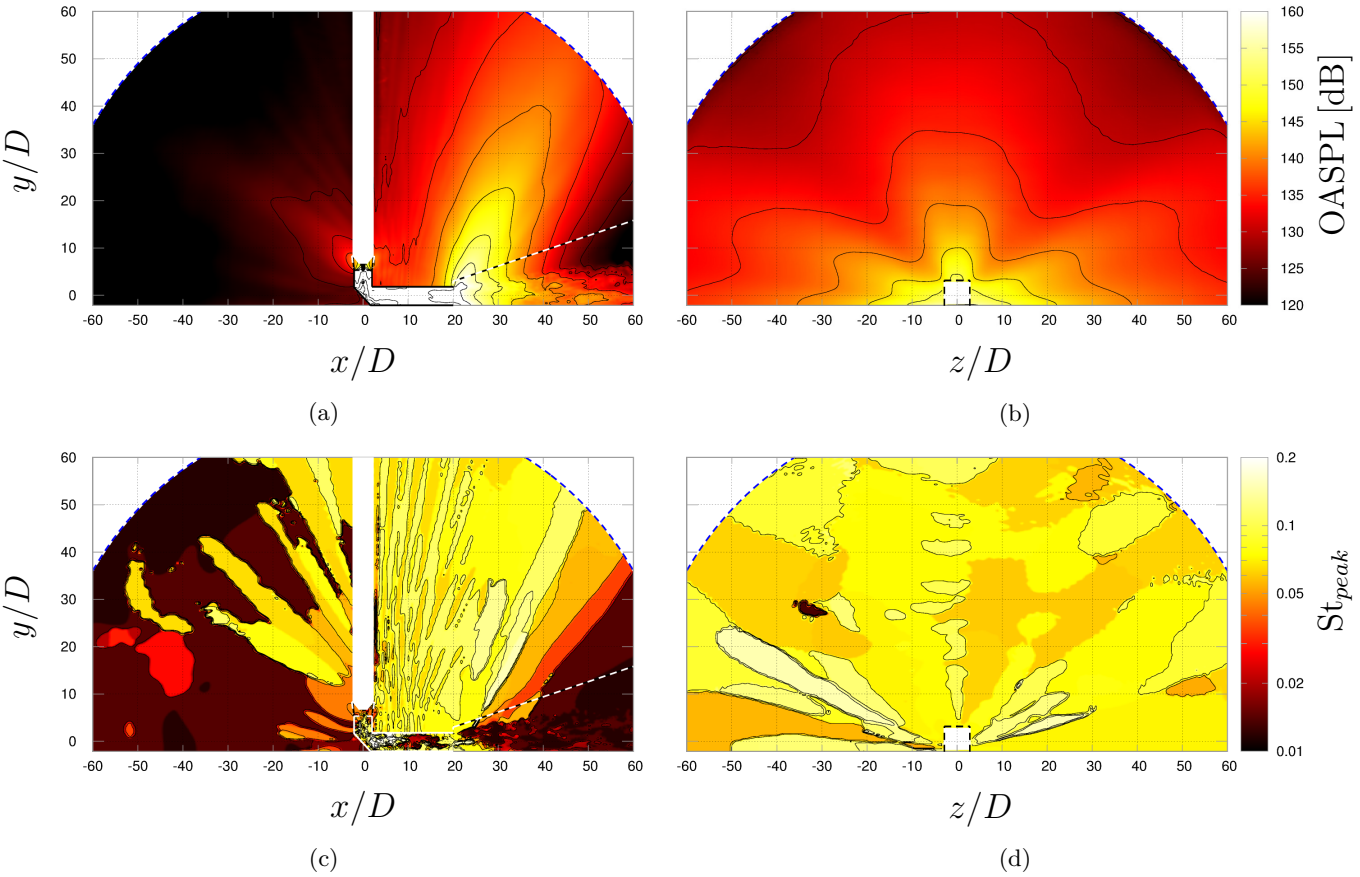

FIG. 14. (Color online) Fields of OASPL (a), (b) and pressure spectrum peak frequency (c), (d) in the planes $\vec{x}\vec{y}(z = 0)$ and $\vec{y}\vec{z}(x = 20D)$. Iso-contours are plotted every 5 dB for the OASPL and for St $\in$ [0.015, 0.03, 0.045, 0.06, 0.09, 0.11, 0.14, 0.17, 0.20] for the frequency as solid black lines. The coupling interface is represented as a dashed black line and the boundary of the refined computational domain as a dashed blue line.

nonlinear effects are predominant over the atmospheric viscous damping. It should be stressed that the pressure derivative skewness $Sk(\dot{p})$ and kurtosis $Kt(\dot{p})$ are usually considered as more sensitive to nonlinear effects than the raw pressure metrics $Sk(p)$ and $Kt(p)$[4,47]. The Goldberg number[3] is defined by

$$\Gamma = \frac{\beta \omega p' \lambda}{\rho_\infty c_\infty^3 \alpha} \tag{4}$$

where $\beta = (1 + \gamma)/2$ is the nonlinearity coefficient, ω the frequency, λ the considered wavelength, and α the dimensionless atmospheric damping depending on the frequency according to the standard ISO-9613[44]. The relative humidity is arbitrarily set to 50% to calculate α. The propagation is nonlinear when $\Gamma \gg 1$. The WSF is defined as the modulus of the average negative slope divided by the average positive slope of the signal wave-

form[3]. The reference value WSF = 1 corresponds to a pure harmonic waveform and WSF = 0 to a perfect sawtooth waveform. It decreases when the nonlinear effects are predominant over the atmospheric viscous damping. The ASF is simply defined as the inverse of WSF and is sometimes preferred for its more convenient dynamic[48].

Four of these metrics are displayed in the plane $\vec{x}\vec{y}(z = 0)$ in Figure 15. The peak frequency of the pressure spectrum is chosen to compute the Goldberg number Γ in Figure 15(a). Values of Γ typically greater than 300 on the coupling interface S2 and greater than 50 (first iso-line) in the far field in the direction of dominant radiation are found which implies that the acoustic levels are high enough to trigger the nonlinear effects. It also suggests that the waves reaching the motor body could be subject to nonlinearities. However, their significance and actual impact on the pressure waveforms can be debated. Hamilton[49] recommends the use of an effective Goldberg number Λ to take into account the wave divergence during the propagation. Far smaller values of Λ compared to Γ would have been reached considering a cylindrical or spherical spreading hypothesis, indicating that cumulative nonlinear effects are probably not important enough to lead to shock formation far from the source once the waves are in a spherical-spreading regime. This point is consistent with the findings of Baars *et al.*[50] regarding the existing laboratory-scale studies. Nevertheless, distortion phenomena are still occurring as clearly highlighted by other metrics. The fields of ASF and $Sk(\dot{p})$ in Figures 15(b) and 15(c) show increasing values along the propagation path within a corridor in the direction of dominant radiation. For each metric, a peak is met before the boundary of the resolved domain at $r_{sph} = 70D$. A similar result is observed with the kurtosis of the pressure derivative $Kt(\dot{p})$ in Figure 15(d) but several spots are additionally accentuated in the acoustic near field. This same behavior has been noticed in the near field of the free jet case[27] and has been associated with localized sharp pressure rises and drops distinct from the cumulative effects. The fields of $Sk(p)$ and $Kt(p)$ (not shown) do not present a satisfactory dynamic to discern the nonlinearities since identical maximum values are reached in the $x < 0$ region where the acoustics levels and Goldberg numbers are incompatible with significant cumulative effects. It confirms that the metrics based on the pressure derivative are more appropriate for characterizing the cumulative nonlinearities while the distortion of the raw pressure probability distribution is mainly driven by the noise sources as explained by Pineau and Bogey[23].

The four quantities $\Gamma(\mathrm{St} = 0.06)$, $\mathrm{ASF}(p)$, $Sk(\dot{p})$, and $Kt(\dot{p})$ are plotted in Figure 16 to compare the Euler simulation with the experiment on the array AZ1. Knowing that the time sampling rate can influence the statistical properties[4], the numerical signals have been degraded to match the experimental sampling $\Delta t = 1 \times 10^{-5}$ s. In practice, the bias has turned out to be rather marginal because of the far more limited cut-off frequency in the computation. The experimental trends are recovered for all metrics with a peak angle around $\theta = 50°$ which is consistent with the maximum in OASPL in Figure 9(a). The Goldberg number profile presents a good agreement with the experiment due to the correspondence in SPL at St = 0.06 since α is assumed identical. On the contrary, the levels of $Sk(\dot{p})$ and $Kt(\dot{p})$ are not well estimated. The discrepancies are attributed to a lack of resolved high frequencies, in other words because of the limited cut-off frequency. This conclusion is corroborated by the better agreement regarding the ASF. This metric, as well as the WSF, is indeed more sensitive to low frequencies[48] than $Sk(\dot{p})$ and $Kt(\dot{p})$. Given that the wave steepening results in an energy transfer to higher frequencies, it also explains why the maximum deviation from the experiment takes place around the peak radiation angle. Based on the Goldberg number and the ASF, the cumulative nonlinear effects are thus considered to be properly predicted over the resolved frequency range but the predictivity remains limited by the cut-off frequency for the other metrics.

The same metrics obtained from the FW-H computation on grid A are appended in Figure 16 for completeness. As expected, Γ presents a shifted peak compared to the experiment because of the shift exhibited in Figure 9(a). In contrast to the Euler simulation, no peak of $Sk(\dot{p})$, $Kt(\dot{p})$ and $\mathrm{ASF}(p)$ are found. An analogous finding has been obtained in the free jet case[27]. It confirms that significant nonlinear effects occurred in the far field and that the Euler approach greatly contributes to the fidelity of the overall simulation. Moreover, if the use of a full Euler solver appears already necessary on this reduced-scale configuration, it will be essential when actual launch pads will be treated since the degree of nonlinearity is expected to increase at full-scale[50].

V. CONCLUSION

In this numerical study, the noise from a hot $M = 3.1$ supersonic jet impinging on a deflector inside a flame trench is simulated. A recently implemented two-way Navier-Stokes−Euler coupling approach is successfully adapted to this realistic launch pad configuration corresponding to an experiment conducted at the MARTEL facility. The validated numerical methodology includes a fine meshing, a geometrical tripping of the turbulence at the convergent wall, and locally defined high-order elements in the full Euler solver.

The established flow analysis shows that the velocity field of the jet before the impingement is affected by the confinement and the massive air suction induced at the trench inlet. Minor grid effects are noticed regarding the mean flow. However, only the present simulation including the turbulence tripping allows a proper turbulence development in the shear layer and a reasonable agreement with the fluctuating velocity measurements operated on the equivalent free jet case. Fully established turbulence spectra are found downstream of the impingement in the horizontal duct.

The acoustic field is then discussed. The trench exit is identified as the main noise source which radiates in

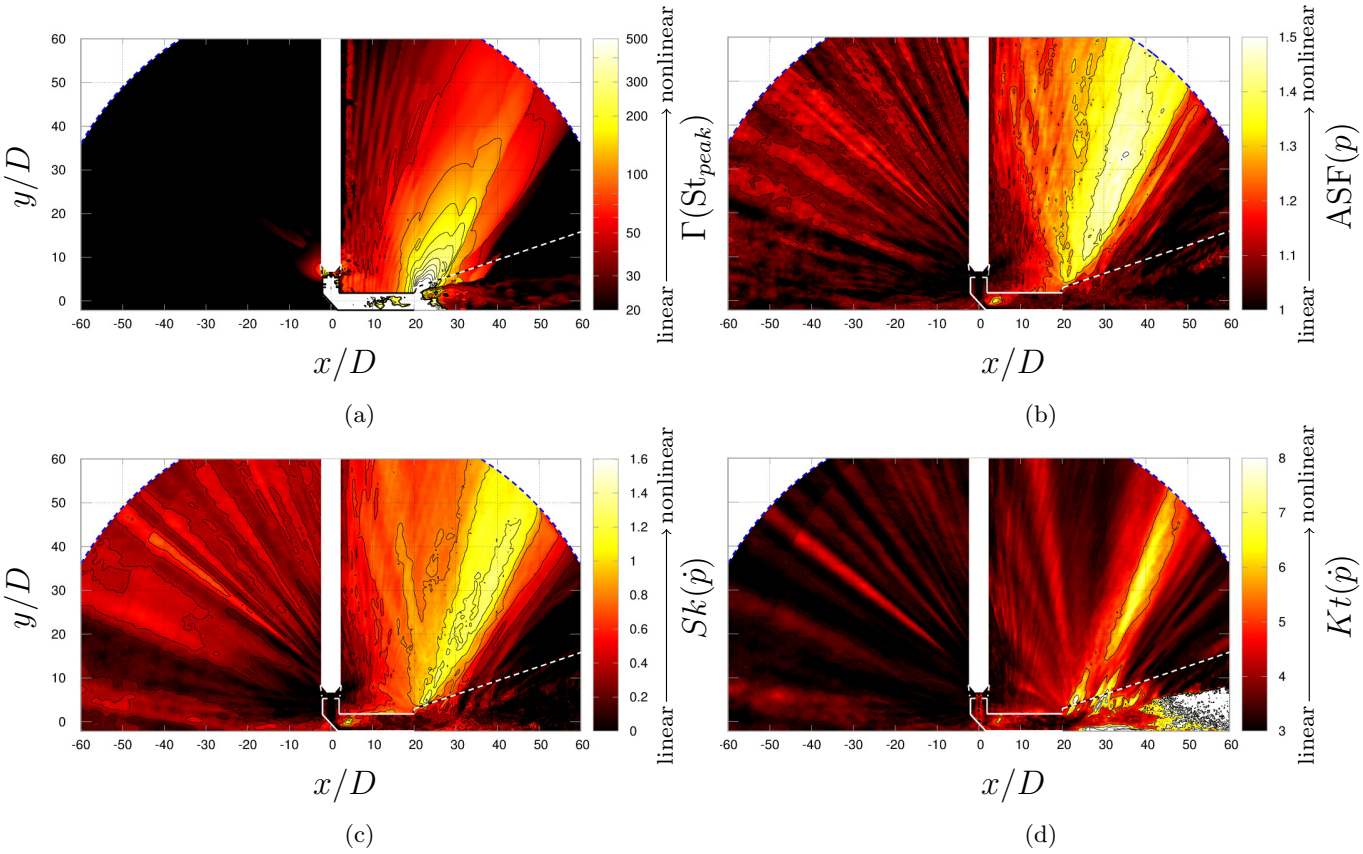

FIG. 15. (Color online) Fields of nonlinearity metrics in the plane $\vec{x}\vec{y}(z=0)$, including the Goldberg number at the pressure spectrum peak frequency (a), the average steepening factor (b), the pressure derivative skewness (c), and the pressure derivative kurtosis (d). Iso-contours are plotted as solid black lines. The coupling interface is represented as a dashed black line and the boundary of the refined computational domain as a dashed blue line.

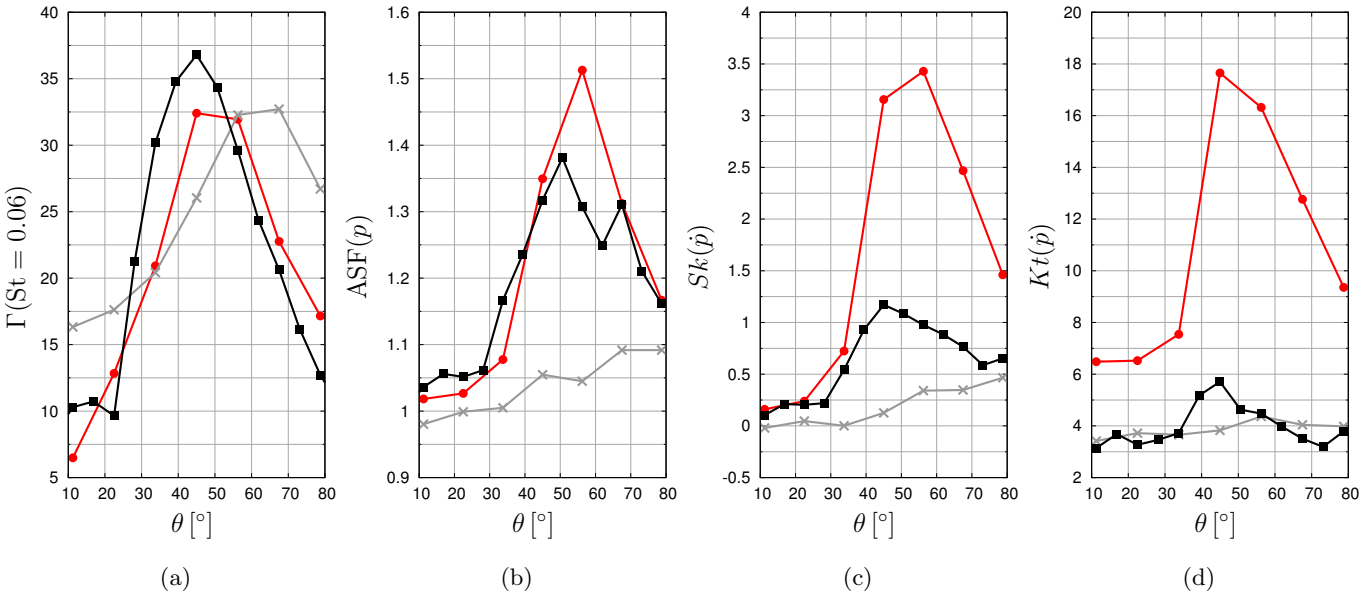

FIG. 16. (Color online) Nonlinearity metrics on the array AZ1, including the Goldberg number at the frequency St = 0.06 (a), the average steepening factor (b), the pressure derivative skewness (c), and the pressure derivative kurtosis (d), for the experimental data (red line with dots), the previous simulation with the FW-H approach (gray line with crosses), and the present simulation with the Euler solver (black line with squares).

multiple dominant directions in the downstream region. Very good agreement between the noise measurements and the Euler simulation is pointed out. Most of the overall sound pressure levels are recovered within a 2 dB error, both in the near field and the far field. Complex installation effects are highlighted including reflection, diffraction, and interference phenomena associated with the ground, the trench or the motor body walls. In particular, the drops in level behind the motor body are well reproduced while the Ffowcs Williams and Hawkings approach does not capture this behavior. The frequency content of the noise is checked by comparing the power spectral densities and appears to be finely predicted.

Taking a closer look at the pressure field inside the duct, the transverse acoustic modes are found to be favored. It results in broadband peaks around specific frequencies in the spectra. These peaks are then recovered in the whole acoustic field at close frequencies, particularly in the range $0.05 < \mathrm{St} < 0.16$ in the directions of dominant radiation. The analysis suggests that the frequency content of the noise keeps the trace of the particular duct mode frequencies in the far field.

The cumulative nonlinear effects are finally examined thanks to a set of metrics from the literature. As expected with acoustic levels higher than 160 dB at the trench exit, the Goldberg number exhibits values that demonstrate a nonlinear propagation regime. However, these findings must be put into the perspective of the acoustic wave divergence. The use of an effective Goldberg number taking into account the cylindrical or the spherical spreading would have led to far smaller values. Significant distortion effects are nevertheless detected in the far field by the pressure derivative skewness and kurtosis, as well as by the average steepening factor. These metrics are employed to compare the experimental and numerical signals. A satisfactory match is obtained with the most sensitive quantities to low frequencies which stresses out that the cut-off frequency is here the main limitation in accurately reproducing the nonlinearities.

The degree of nonlinearity and the geometrical complexity are finally expected to increase at larger scales. The present Navier-Stokes−Euler coupling on unstructured grids thus appears appropriate to predict the acoustic environment at lift-off on real launch pads.

ACKNOWLEDGMENTS

This study was supported by the French national space agency CNES and ONERA's scientific direction. The authors are grateful to Ch. Bailly from LMFA, École Centrale de Lyon for his scientific support, P. Noir from CNES for his financial support to the project, and Ch. Peyret, G. Chaineray, and E. Quémerais from ONERA for their work on the CEDRE-SPACE two-way coupling possibilities.

[1]C. Bailly and K. Fujii, "High-speed jet noise," Mech. Eng. Rev. **3**(1), 15–00496 (2016) doi: 10.1299/mer.15-00496.

[2]C. Tam, K. Viswanathan, K. Ahuja, and J. Panda, "The source of jet noise: Experimental evidence," J. Fluid Mech. **615**, 253–292 (2008) doi: 10.1017/S0022112008003704.

[3]W. Baars, C. Tinney, M. Wochner, and M. Hamilton, "On cumulative nonlinear acoustic waveform distortions from high-speed jets," J. Fluid Mech. **749**, 331–366 (2014) doi: 10.1017/jfm.2014.228.

[4]P. Mora, N. Heeb, J. Kastner, E. Gutmark, and K. Kailasanath, "Impact of heat on the pressure skewness and kurtosis in supersonic jets," AIAA J. **52**(4), 777–787 (2014) doi: 10.2514/1.J052612.

[5]B. Mercier, T. Castelain, and C. Bailly, "Experimental characterisation of the screech feedback loop in underexpanded round jets," J. Fluid Mech. **824**, 202–229 (2017) doi: 10.1017/jfm.2017.336.

[6]A. Krothapalli, E. Rajkuperan, F. Alvi, and L. Lourenco, "Flow field and noise characteristics of a supersonic impinging jet," J. Fluid Mech. **392**, 155–181 (1999) doi: 10.1017/S0022112099005406.

[7]M. Akamine, K. Okamoto, K. Gee, T. Neilsen, S. Teramoto, T. Okunuki, and S. Tsutsumi, "Effect of nozzle-plate distance on acoustic phenomena from supersonic impinging jet," AIAA J. **56**(5), 1943–1952 (2018) doi: 10.2514/1.J056504.

[8]P. Malbéqui, R. Davy, and C. Bresson, "Experimental characterization of the acoustics of the future Ariane 6 launch pad," in *7^{th} European Conference for Aeronautics and Space Sciences*, SD1-3.4-38, Milano, Italy (2015), doi: 10.13009/EUCASS2017-38.

[9]S. Tsutsumi, T. Ishii, K. Ui, S. Tokudome, and K. Wada, "Study on acoustic prediction and reduction of Epsilon launch vehicle at liftoff," J. Spacecraft Rockets **52**(2), 350–361 (2015) doi: 10.2514/1.A33010.

[10]S. Tsutsumi, "Design of launch pad for mitigating acoustic loads on launch vehicle at liftoff," J. Acoust. Soc. Korea **39**(4), 331–341 (2020) doi: 10.7776/ASK.2020.39.4.331.

[11]J. Varnier, V. Koudriavstsev, and A. Safronov, "Simplified approach of jet aerodynamics with a view to acoustics," AIAA J. **44**(7), 1690–1693 (2006) doi: 10.2514/1.5087.

[12]G. Brès and S. Lele, "Modelling of jet noise: a perspective from large-eddy simulations," Philos. Trans. R. Soc. A **377**(2159), 20190081 (2019) doi: 10.1098/rsta.2019.0081.

[13]C. Bogey, O. Marsden, and C. Bailly, "Influence of initial turbulence level on the flow and sound fields of a subsonic jet at a diameter-based Reynolds number of 10^5," J. Fluid Mech. **701**, 352–385 (2012) doi: 10.1017/jfm.2012.162.

[14]G. Brès, P. Jordan, V. Jaunet, M. Le Rallic, A. Cavalieri, A. Towne, S. Lele, T. Colonius, and O. Schmidt, "Importance of the nozzle-exit boundary-layer state in subsonic turbulent jets," J. Fluid Mech. **851**, 83–124 (2018) doi: 10.1017/jfm.2018.476.

[15]R. Gojon, C. Bogey, and O. Marsden, "Investigation of tone generation in ideally expanded supersonic planar impinging jets using large-eddy simulation," J. Fluid Mech. **808**, 90–115 (2016) doi: 10.1017/jfm.2016.628.

[16]A. Dauptain, L. Gicquel, and S. Moreau, "Large eddy simulation of supersonic impinging jets," AIAA J. **50**(7), 1560–1574 (2012) doi: 10.2514/1.J051470.

[17]C. Brehm, J. Housman, and C. Kiris, "Noise generation mechanisms for a supersonic jet impinging on an inclined plate," J. Fluid Mech. **797**, 802–850 (2016) doi: 10.1017/jfm.2016.244.

[18]T. Nonomura, Y. Goto, and K. Fujii, "Aeroacoustic waves generated from a supersonic jet impinging on an inclined flat plate," Int. J. Aeroacoust. **10**(4), 401–425 (2011) doi: 10.1260/1475-472X.10.4.401.

[19]T. Nonomura, H. Honda, Y. Nagata, M. Yamamoto, S. Morizawa, S. Obayashi, and K. Fujii, "Plate-angle effects on acoustic waves from supersonic jets impinging on inclined plates," AIAA J. **54**(3), 816–827 (2016) doi: 10.2514/1.J054152.

[20]G. Rahier, J. Prieur, F. Vuillot, N. Lupoglazoff, and A. Biancherin, "Investigation of integral surface formulations for acoustic post-processing of unsteady aerodynamic jet simulations," Aerosp. Sci. Technol. **8**(6), 453–467 (2004) doi: 10.1016/j.ast.2004.04.005.

[21] J. Troyes, F. Vuillot, H. Lambaré, and A. Espinosa Ramos, "Study of impinging supersonic jet noise with aerodynamics and acoustics numerical simulations," in *30th International Symposium on Space Technology and Science*, 2015-399, Kobe-Hyogo, Japan (2015).

[22] N. de Cacqueray and C. Bogey, "Noise of an overexpanded Mach 3.3 jet: Non-linear propagation effects and correlations with flow," Int. J. Aeroacoust. **13**(7&8), 607–632 (2014) doi: 10.1260/1475-472X.13.7-8.607.

[23] P. Pineau and C. Bogey, "Numerical investigation of wave steepening and shock coalescence near a cold mach 3 jet," J. Acoust. Soc. Am. **149**(1), 357–370 (2021) doi: 10.1121/10.0003343.

[24] O. Labbé, C. Peyret, G. Rahier, and M. Huet, "A CFD/CAA coupling method applied to jet noise prediction," Comput. Fluids **86**, 1–13 (2013) doi: 10.1016/j.compfluid.2013.07.013.

[25] V. Sassanis, A. Sescu, E. Collins, R. Harris, and E. Luke, "A hybrid approach for nonlinear computational aeroacoustics predictions," Int. J. Comput. Fluid D. **31**(1), 1–20 (2017) doi: 10.1080/10618562.2016.1274399.

[26] A. Langenais, F. Vuillot, C. Peyret, G. Chaineray, and C. Bailly, "Assessment of a two-way coupling methodology between a flow and a high-order nonlinear acoustic unstructured solvers," Flow Turbul. Combust. **101**(3), 681–703 (2018) doi: 10.1007/s10494-018-9928-0.

[27] A. Langenais, F. Vuillot, J. Troyes, and C. Bailly, "Accurate simulation of the noise generated by a hot supersonic jet including turbulence tripping and nonlinear acoustic propagation," Phys. Fluids **31**(1), 016105 (2019) doi: 10.1063/1.5050905.

[28] J. Troyes, F. Vuillot, A. Langenais, and H. Lambaré, "Coupled CFD-CAA simulation of the noise generated by a hot supersonic jet impinging on a flat plate with exhaust hole," in *25th AIAA/CEAS Aeroacoustics Conference*, Delft, Netherlands (2019), doi: 10.2514/6.2019-2752.

[29] D. Gély, J.-C. Valière, H. Lambaré, and H. Foulon, "Overview of aeroacoustic research activities in MARTEL facility applied to jet noise," in *35th International Congress and Exposition on Noise Control Engineering*, Honolulu, HI, USA (2006).

[30] A. Langenais, F. Vuillot, J. Troyes, and C. Bailly, "Numerical investigation of the noise generated by a rocket engine at lift-off conditions using a two-way coupled CFD-CAA method," in *23rd AIAA/CEAS Aeroacoustics Conference*, 2017-3212, Denver, CO, USA (2017), doi: 10.2514/6.2017-3212.

[31] J. Troyes, F. Vuillot, A. Langenais, H. Lambaré, and P. Noir, "Large-eddy simulations of launcher lift-off noise and comparisons to experiments on model flame trenches," in 174th *Meeting of the Acoustical Society of America*, New Orleans, LA, USA (2017), Vol. 142, doi: 10.1121/1.5014091.

[32] A. Refloch, B. Courbet, A. Murrone, P. Villedieu, C. Laurent, P. Gilbank, J. Troyes, L. Tessé, G. Chaineray, J.-B. Dargaud, E. Quémerais, and F. Vuillot, "CEDRE software," Aerosp. Lab J. **2**, AL02–11 (2011) https://hal.archives-ouvertes.fr/hal-01182463.

[33] D. Scherrer, F. Chedevergne, P. Grenard, J. Troyes, A. Murrone, E. Montreuil, F. Vuillot, N. Lupoglazoff, M. Huet, B. Sainte-Rose, Sainte-Rose, N. Bertier, J.-M. Lamet, T. Le Pichon, E. Radenac, A. Nicole, L. Matuszewski, and M.-P. Errera, "Recent CEDRE applications," Aerosp. Lab J. **2**, AL02–13 (2011) https://hal.archives-ouvertes.fr/hal-01182477.

[34] F. Haider, B. Courbet, and J.-P. Croisille, "A high-order interpolation for the finite volume method: The coupled least squares reconstruction," Comput. Fluids **176**, 20–39 (2018) doi: 10.1016/j.compfluid.2018.09.009.

[35] E. Toro, *Riemann Solvers and Numerical Methods for Fluid Dynamics* (Springer Berlin Heidelberg, 2009).

[36] P. Delorme, P. Mazet, C. Peyret, and Y. Ventribout, "Computational aeroacoustics applications based on a discontinuous Galerkin method," C.R. Mécanique **333**(9), 676–682 (2005) doi: 10.1016/j.crme.2005.07.007.

[37] E. Quémerais, "Coupling with interpolation parallel interface" , ONERA web site (2016), https://w3.onera.fr/cwipi/.

[38] R. Fontaine, G. Elliott, J. Austin, and J. Freund, "Very near-nozzle shear-layer turbulence and jet noise," J. Fluid Mech. **770**, 27–51 (2015) doi: 10.1017/jfm.2015.119.

[39] T. Nonomura, H. Nakano, Y. Ozawa, D. Terakado, M. Yamamoto, K. Fujii, and A. Oyama, "Large eddy simulation of acoustic waves generated from a hot supersonic jet," Shock Waves **29**(8), 1133–1154 (2019) doi: 10.1007/s00193-019-00895-2.

[40] C. Bogey and O. Marsden, "Identification of the effects of the nozzle-exit boundary-layer thickness and its corresponding Reynolds number in initially highly disturbed subsonic jets," Phys. Fluids **25**(5), 055106 (2013) doi: 10.1063/1.4807071.

[41] J. Liu, K. Kailasanath, J. Boris, N. Heeb, D. Munday, and E. Gutmark, "Effect of the initial turbulence level on an under-expanded supersonic jet," AIAA J. **51**(3), 741–745 (2013) doi: 10.2514/1.J051949.

[42] M. Lorteau, F. Cléro, and F. Vuillot, "Analysis of noise radiation mechanism in hot subsonic jet from a validated large eddy simulation solution," Phys. Fluids **27**(7), 075108 (2015) doi: 10.1063/1.4926792.

[43] R. Léger, C. Peyret, and S. Piperno, "Coupled discontinuous Galerkin / finite difference solver on hybrid meshes for computational aeroacoustics," AIAA J. **50**(2), 338–349 (2012) doi: 10.2514/1.J051110.

[44] "ISO 9613-1:1993 - Acoustics - Attenuation of sound during propagation outdoors - Part 1: Air absorption" (1993).

[45] C. Tam, S. Parrish, and K. Viswanathan, "Harmonics of jet screech tones," AIAA J. **52**(11), 2471–2479 (2014) doi: 10.2514/1.J052850.

[46] J. Troyes, F. Vuillot, H. Lambaré, and A. Espinosa Ramos, "Numerical study of free supersonic hot jet on unstructured grids with emphasis on aerodynamics and resulting radiated noise," in *22nd AIAA/CEAS Aeroacoustics Conference*, 2016-2734, Lyon, France (2016), doi: 10.2514/6.2016-2734.

[47] B. Reichman, M. Muhlestein, K. Gee, T. Neilsen, and D. Thomas, "Evolution of the derivative skewness for nonlinearly propagating waves," J. Acoust. Soc. Am. **139**(3), 1390–1403 (2016) doi: 10.1121/1.4944036.

[48] M. Muhlestein, K. L. Gee, T. Neilsen, and D. Thomas, "Evolution of the average steepening factor for nonlinearly propagating waves," J. Acoust. Soc. Am. **137**(2), 640–650 (2015) doi: 10.1121/1.4906584.

[49] M. Hamilton, "Effective Gol'dberg number for diverging waves," J. Acoust. Soc. Am. **140**(6), 4419–4427 (2016) doi: 10.1121/1.4968787.

[50] W. Baars, C. Tinney, and M. Hamilton, "Piecewise-spreading regime model for calculating effective Gol'dberg numbers for supersonic jet noise," AIAA J. **54**(9), 2833–2842 (2016) doi: 10.2514/1.J054790.